



# Investigation of Seismic Anisotropy in the Undisturbed Rotondo Granite

Kathrin Behnen<sup>1</sup>, Marian Hertrich<sup>1</sup>, Hansruedi Maurer<sup>1</sup>, Alexis Shakas<sup>1</sup>, Kai Bröker<sup>2</sup>, Claire Epiney<sup>3</sup>, María Blanch Jover<sup>4</sup>, and Domenico Giardini<sup>1</sup>

<sup>1</sup>Department of Earth Sciences, ETH Zürich, Sonneggstrasse 5, 8092 Zürich, Switzerland

<sup>2</sup>Centre for Hydrogeology and Geothermics (CHYN), University of Neuchâtel, Rue Emile Argand 11, 2000 Neuchâtel, Switzerland

<sup>3</sup>Geo-Energie Suisse AG, Reitergasse 11, 8004 Zürich, Switzerland

<sup>4</sup>Geomar, Wischhofstrasse 1-3, 24148 Kiel, Germany

**Correspondence:** Kathrin Behnen (kathrin.behnen@erdw.ethz.ch)

**Abstract.** The hypothesis of stress-induced seismic anisotropy was tested in the Bedretto Lab, a deep underground rock laboratory in the Swiss alps. Several comprehensive crosshole seismic surveys were acquired to analyze the directional dependency of seismic wave velocities in the undisturbed host rock. This required precise knowledge on the source and receiver positions as well as a good data quality that allow the determination of traveltimes for different wave types. A tilted transverse isotropic (TTI) model could be established that explains the measured data to a first order. All relevant model parameters could be well constrained using P- and S-wave arrival times. However, a systematic misfit distribution indicates that a more complex anisotropy model might be required to fully explain the measurements. This is consistent with our hypothesis that seismic anisotropy has a significant stress-induced component. More controlled laboratory experiments on the centimeter to decimeter scale were performed to validate our field measurements. These measurements show a comparable order of P- and S-wave anisotropy in the rock volume. The knowledge on the driving mechanism for anisotropy in igneous rocks can potentially help to enhance the monitoring of stress field variations during geothermal operations, thereby improving hazard assessment protocols.

## 1 Introduction

The importance of seismic anisotropy, hereafter referred to as anisotropy, is well known and studied for decades. Neglecting anisotropy in seismic imaging can result in significant errors in terms of traveltime calculations and ray path determinations. Examples on exploration scale include Eken et al. (2012); Daley and Hron (1977) and Thomsen (1986). Also in engineering applications, it is important to consider anisotropy as it affects the stability of excavations and boreholes, rock-cutting performance and fracture propagation (Heng et al., 2015; Lee et al., 2012; Özbek et al., 2018).

Aligned minerals, foliation, fractures, faults, bedding of a rock and the in-situ stress field are known to cause seismic anisotropy in rocks (Barton, 2006; Al-Harathi, 1998; Song et al., 2004; Chan and Schmitt, 2015; Nur and Simmons, 1969; Sayers, 2002). The type of rock (sedimentary, igneous or metamorphic) as well as the considered scale are decisive to determine which pa-



rameters control the elastic behaviour of the rock. Anisotropy of sedimentary rocks is often controlled by the internal bedding of the rock or alignment of minerals, while metamorphic rocks often show a foliation depending on the stress field while the rock was formed (Horne, 2013; Thomsen, 1986; Heng et al., 2015; Özbek et al., 2018). The controlling parameter can also vary on different scales, so that a fault zone can be the dominating feature on a regional scale but mineral alignment can control the wave propagation on smaller samples of the same rock volume.

Most anisotropy studies have been carried out on sedimentary or metamorphic rocks, as these rock types are expected to have higher anisotropy (Al-Harhi, 1998). However, also igneous rocks can have a significant anisotropy, which should be incorporated, especially if the rocks are jointed or disturbed by fault zones (Ramamurthy et al., 1993). While both, the source of anisotropy as well as the direction of the faster velocity is often obvious in sedimentary or metamorphic rocks, it might be harder to detect the symmetry direction and controlling parameters in igneous rocks.

In our study, we analyse the anisotropy of an undisturbed igneous rock in an underground laboratory. Such laboratories provide the opportunity for in-situ experiments for research on geenergy, nuclear waste disposal, earthquake nucleation or engineering aspects (Plenkens et al., 2023; Ma et al., 2022). All these potential application can benefit from the realistic scale that such laboratories offer (compared to small-scale laboratory experiments) (Gischig et al., 2020). In addition, we can compare our results with previous analyses on the geology, fracture network and stress field around the test volume. Especially the link of the anisotropy to fractures and stress is highly important for the characterization of a geothermal reservoir, as these parameter control the reservoir creation and fluid flow during geothermal production (Amann et al., 2018).

In this contribution, we characterize the anisotropy of the rock volume of interest by active seismic measurements in three differently oriented boreholes. We evaluate the known sources of anisotropy by comparing our results to the other measurement campaigns and identify the controlling parameter in the undisturbed igneous rock.

The paper is structured as followed: In the first part, the required theory used to describe the anisotropy is explained. Then the laboratory itself and the performed measurement campaigns are introduced. In the end, the resulting model is explained and analysed and the results are discussed in a bigger context, comparing our results with other data sets.

## 2 Theory

The most common type of anisotropy in earth's structures is a (tilted) transverse isotropic medium (TTI). Such a medium is characterized by a velocity  $v_0$  in the direction of a symmetry axis and a rotational symmetric velocity distribution around it, resulting in a symmetry plane of (usually) higher velocity perpendicular to it. A TTI medium, or hexagonal material, is one of the simplest forms of anisotropy that can be used in geophysical applications and is well studied (Carcione et al., 1988; Thomsen, 1986). We therefore also start approximating our measurement data with a TTI medium.

The mathematical framework to describe such a medium is given, for example, in Daley and Hron (1977). They state that the velocity field in a TTI medium can be fully described by the five independent parameters  $C_{ij}$  of the elastic tensor and the density of the rock  $\rho$ . For the calculation of the velocity in a specific direction, also the inclination angle  $\xi$  between the wave front normal and the symmetry axis must be known. The wave front normal can be described by the azimuth  $\varphi_r$  and dip  $\theta_r$  from source to receiver. So additionally to the unknown elastic tensor parameters  $C_{ij}$  also the orientation of the symmetry axis,



described by azimuth  $\varphi_0$  and dip  $\theta_0$  is unknown in our case.

The phase velocities of the different wave types are then defined as:

$$v_P(\xi) = \sqrt{\frac{1}{2\rho} [C_{33} + C_{55} + (C_{11} - C_{33})\sin^2(\xi) + D(\xi)]} \quad (1)$$

$$v_{S1}(\xi) = C_{66}\sin^2(\xi) + C_{55}\cos^2(\xi) \quad (2)$$

$$60 \quad v_{S2}(\xi) = \sqrt{\frac{1}{2\rho} [C_{33} + C_{55} + (C_{11} - C_{33})\sin^2(\xi) - D(\xi)]} \quad (3)$$

with:

$$D(\xi) = \left[ (C_{33} - C_{55})^2 + 2 \left[ 2(C_{13} + C_{55})^2 - (C_{33} - C_{55})(C_{11} + C_{33} - 2C_{44}) \right] \sin^2(\xi) + \left[ (C_{11} + C_{33} - 2C_{44})^2 - 4(C_{13} + C_{55})^2 \right] \sin^4(\xi) \right]^{1/2} \quad (4)$$

65 The elastic parameters  $C_{ij}$  can also be expressed by the Thomsen parameters  $\alpha_0$ ,  $\beta_0$ ,  $\gamma$ ,  $\epsilon$  and  $\delta$ . These parameters are defined by Thomsen (1986) as:

- $\alpha_0$ : P-wave velocity along the symmetry axis  $\sqrt{C_{33}/\rho}$
- $\beta_0$ : S-Wave velocity along the symmetry axis  $\sqrt{C_{55}/\rho}$
- $\gamma$ : fractional difference between vertical and horizontal S1-Wave velocity  $((C_{66} - C_{55})/2C_{55})$
- 70 -  $\delta$ : controlling parameter for near-vertical rays  $((C_{13} + C_{55})^2 - (C_{33} - C_{55})^2)/(2C_{33}(C_{33} - C_{55}))$
- $\epsilon$ : fractional difference between vertical and horizontal P-Wave velocity  $(C_{11} - C_{33})/2C_{33}$

The advantage of these parameters is that they have a direct physical meaning and are much easier to interpret. We use equation 1 to3, with  $C_{ij}$  expressed by the Thomsen parameters.

75 Unlike in an isotropic medium, the S wave velocity does not only depend on its propagation direction but also on its polarization direction. This causes a splitting of the S wave in a faster and a slower wave, described by equation 2 and 3. This splitting clearly indicates that the medium of interest is anisotropic.

We determine the Thomsen parameters by minimizing the weighted L2-norm of the different wave forms. For that purpose, we consider the first arriving P waves and the arriving of both, the faster S1 wave and the slower S2 wave. We assume that the velocity distribution in  
80 the medium of interest is sufficiently homogeneous, such that a straight ray assumption is justified, that is, the predicted travel times are the source-receiver distances divided by the velocity along the straight ray. The arrival times of the P-waves are most accurate, so the L2-norm of the P-wave misfit is weighted higher compared to the L2-norm of the different S-waves. By this, we ensure that the resulting model is not biased by outliers in the S-wave picks.

The reliability of the estimated Thomsen parameters is important for the interpretation of the results. This can be estimated with tools from  
85 linear inverse theory. Here, we consider the model resolution matrix  $\mathbf{R}$ , relating the true model parameter  $\mathbf{m}^{\text{true}}$  to the estimated parameter  $\mathbf{m}^{\text{est}}$ . The relative values on the diagonal of  $\mathbf{R}$  give an estimate how well we can determine the different parameters. The off-diagonal values show trade-offs between the different parameters and thus reveal dependencies between the model parameters.



**Table 1.** Overview over the different boreholes used for this survey.

Borehole Name	TM	Length	Dip	Azimuth
SB2.1	2066	30 m	89°	150°
SB2.2	2075	40 m	60°	226°
SB2.3	2094	40 m	71°	134°

We follow the definition of Menke (2018) to calculate  $\mathbf{R} = (\mathbf{G}^T \mathbf{G} + \lambda \mathbf{1})^{-1} \mathbf{G}^T \mathbf{G}$ . Matrix  $\mathbf{G}$  includes the sensitivities of the data points  $d_i$  ( $d = t_P, t_{S1}, t_{S2}$ ) with respect to the model parameters  $m_j = \alpha, \beta, \gamma, \delta, \epsilon, \varphi_0$  and  $\theta_0$ :

$$90 \quad G_{ij} = \frac{\partial d_i}{\partial m_j}. \quad (5)$$

### 3 Site Description

The Bedretto Underground Laboratory for Geoennergies and Geosciences (Bedretto Lab) is located in southern Switzerland in the canton of Ticino. It is located in a 5.2 km long tunnel that connects the Bedretto Valley with the Furka Base Tunnel, crossing from west to north-east. Originally build as auxiliary tunnel for the construction of the Furka railway tunnel, it is now maintained and operated by ETH Zurich.

95 The Bedretto Lab was established to study techniques and ongoing processes during the production and operation of Enhanced Geothermal Systems (EGS) (Rast et al., 2022). The main niche of the lab is located at tunnel meter (TM) 2000 to 2100 m from the southern tunnel entrance with an approximate overburden of 1000m (Bröker and Ma, 2022). The host rock of the lab is a mostly homogeneous granitic intrusion, the Rotondo granite. This geological setting is close to real EGS reservoir conditions which is important to upscale the results of the different studies Gischig et al. (2020).

100 The Bedretto Lab hosts several boreholes of different lengths, partly equipped with permanently installed sensors. An overview over the lab and the boreholes is shown in Fig. 1. For this study, the boreholes SB2.1, SB2.2 and SB2.3 were used for extensive active seismic surveys. These boreholes are also called "tripod boreholes" as they are pointing downwards in three different directions, spanning a tripod. All three boreholes are water-filled, allowing the use of different seismic equipment, explained in Sect. 4. The penetrated and analyzed Rotondo granite doesn't show any major fault or fracture zones close to the tripod, so that we can assume that the rock volume is homogeneous. The boreholes  
 105 were originally drilled for stress measurements of the background rock so that the stress conditions around the boreholes and the Bedretto Lab in general are well known (Bröker et al., 2024; Bröker and Ma, 2022).

The boreholes are located at the end of the lab niche, at TM 2066 to TM 2094 measured from the southern entrance of the tunnel. The vertical and inclined boreholes have a length of 30m and 40m, respectively and a diameter of 101mm. They are completely water-filled and freely accessible, which allows the usage of different seismic sources and receivers. Detailed information on the borehole orientations are given in

110 Tab. 1.

The borehole trajectories used for the following analyses are based on a combination of logging and laser measurements. Laser measurements allow a highly precise measurement of single points in the boreholes, used to interpolate the trajectories in between. In the lower part of the boreholes, laser measurements were not feasible anymore, as the water in the boreholes couldn't be pumped out of the complete borehole. Instead information on the azimuth and dip from several logging runs in the boreholes were used to determine the trajectory of the boreholes

115 in the lower part. The combination of these two data sets allow a highly precise description of the borehole trajectories which is crucial for anisotropy measurements.

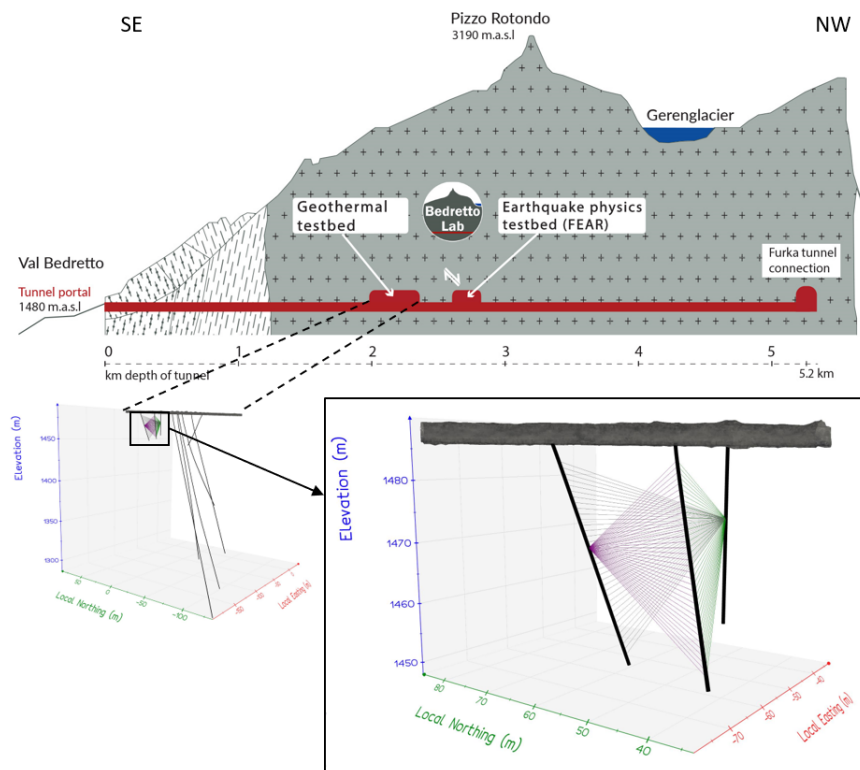


**Figure 1.** The boreholes used SB2.1, SB2.2 and SB2.3 are located in the Bedretto tunnel around TM2000. The boreholes were used for extensive crosshole seismic surveys with different sources and receivers. The purple, grey and green lines show exemplary rays in the three covered planes. Cross section after Keller and Schneider (1982).

**Table 2.** Overview over the different measurement campaigns.

Date	Source Type	Receiver Type	Source Spacing	Receiver Spacing
01./02.12.2021	P-Wave Sparker	Hydrophone Chain	1m	1m
11.05.2022	P-Wave Sparker	Hydrophone Chain	1m	1m
27.03.2023	S-Wave Sparker	Hydrophone Chain	Single Positions	1m
25.05.2023	P-Wave Sparker	3C-Geophone	1m	Single Positions
05./06.07.2023	P-Wave Sparker	3C-Geophone Chain	1m	1m or 2m

#### 4 Measurements

In the boreholes SB2.1, SB2.2 and SB2.3, introduced in Sect. 3, several different seismic crosshole surveys were performed. The boreholes span one straight and two curved planes, allowing the measurement of the wave propagation in several different directions. The location in the tunnel as well as the orientation of the boreholes are also shown in Fig. 1.



The measurements were performed in different campaigns from December 2021 to July 2023. An overview of the measurements is given in Tab. 2. We started with a standard survey, using a P-wave sparker as source and a hydrophone chain as receivers. The P-wave sparker creates a highly repeatable, high-frequency seismic signal by discharging energy through two adjacent electrodes (Geotomographie GmbH). Its radiation characteristics is approximately isotropic. The hydrophones, attached on a chain with 1m spacing, can record pressure signals acting on the sensor from any direction, but the recorded data do not contain information about the incident angle of the seismic signal. The recorded data of the first two surveys (12.2021 and 05.2022) do not only show the arrival of a P-wave, but also of S-waves. This can be explained by a deformation of the source borehole itself, producing not only longitudinal but also transverse waves propagating through the rock. These waves are converted in longitudinal waves when they hit the water of the receiver borehole, acting on the hydrophones. In a next step, we determined the traveltime of the different S-waves in more detail. For that purpose, we employed a S-wave sparker as source, which emits a horizontally polarized, directed S-wave. The data recorded in this survey have a high noise level and do not show the desired signals of S-waves in the recordings, so we did not further consider the S-wave sparker data. Instead we proceeded to record the signal of the P-wave sparker on 3 component (3C) geophones. The geophones were clamped to the borehole wall, which allowed recording both, the P- and S-waves directly on the rock surface on three mutually perpendicular components. Unfortunately, we were not able to determine the orientation of the sensor in the borehole, so that neither a statement about the incident direction of the arriving waves nor an alignment of the sensors towards the source position can be made. After some successful test measurements, we covered most of the test volume with 1m spacing of both, sources and receivers. Solely the edges of the test volume, in the uppermost and lowermost part of the boreholes, we increased the spacing between the receivers to 2m for logistical reasons. The aim of this survey was to further separate the differently polarized S-waves from each other. During the data acquisition we had to face several challenges, such as problems with the triggering of the recordings, the alignment of the sensors in the borehole and an higher overall noise level so that this data set was only used as a comparison to the hydrophone recordings and to verify the arrival time of the S-waves quantitatively. The data analysed in the following include the recordings of the first two surveys, using a P-wave sparker as source and the hydrophone chain as receiver.

## 5 Data Analysis

The wave propagation of a seismic wave is controlled by the properties of the rock it is propagating through. Analyzing the traveltime of the wave from the source to a receiver is a simple way to extract information about these properties. In the following, the recorded data from the first two surveys (Dec. 2021 and May 2022) are presented and analysed to characterize the undisturbed Rotondo granite in the Bedretto Lab. The amplitudes of the P-waves and most of the S-waves are clearly visible in the raw data due to the short distances between source and receiver and a very low noise level in the test volume. The quality of the data was further increased by stacking three shots per position. No frequency filtering was applied. An exemplary receiver gather is shown in Fig. 2 (left) with single waveforms recorded on the hydrophones for selected traces (right). The receiver gather shows the signal recorded on a hydrophone in SB2.2 at 23m depth, for shot positions in SB2.3 from 3 to 38m. The waveforms on the right correspond to the marked traces in the gather at shot positions of 9m, 25m and 32m depth. The same geometrical setup with recordings on the 3C geophones is shown in Fig. A1.

The onset of the P-wave can clearly be identified for all shot positions (P1). The arrival of the S-waves is only visible for longer ray paths (here source position 3 to 20 and 32 to 38, P2), where it is neither covered in the coda of the P-wave nor by reflected waves as it is often the case for deeper shot positions. For some source-receiver orientations a splitting of the S-wave in a faster wave S1 (P2a) and a slower wave

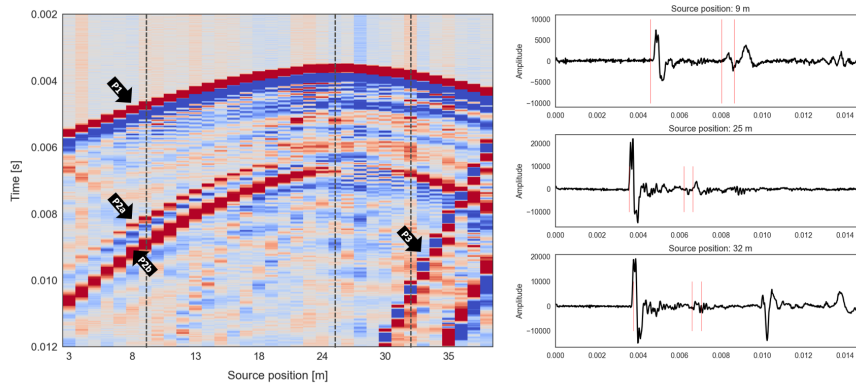


**Figure 2.** *Left:* An exemplary receiver gathern for shot positions in SB2.3 with 1m spacing recorded on a hydrophone in SB2.2 at 23m depth. The onset of the P-wave is clearly visible on all traces (P1). In the left part of the gathern, the splitting of the S-Wave in a fast (P2a) and slow (P2b) S-wave is apparent. For shorter distances between source and receiver, the S-wave gets covered in the coda of the P-wave and the splitting is not visible anymore. In some parts of the signal, also other wave types such as reflected or tube waves are visible (P3), which are not further analysed.

*Right:* The waveforms show the marked traces of the receiver gathern. The red lines represent the expected arrival times. On all three traces, the arrival of the P-wave is clearly visible. On the first trace, the S-waves separate and can be picked. On the second and third trace, the arrival of the different S-waves is less clear and can't be picked accurately.

S2 can be identified (P2b). This is a feature which can only occur in anisotropic media and is already a clear indicator that the tested granite is seismically anisotropic. A separation of different S-waves is mainly identified in the plane between borehole SB2.2 and SB2.3 while only one S-wave can be detected in the other two planes for most source-receiver pairs. In Fig. A2 more examples for different source-receiver geometries are shown for comparison.

160 The receiver gathern in Fig. 2 also shows other wave types such as reflected waves or tube waves for deeper shot positions (P3). These signals are not considered in this study as only the arrival time of the direct waves will be analyzed.

In the next step, the traveltimes for all unambiguous onsets were picked and converted into apparent velocities, thereby assuming straight rays, which was judged to be a valid assumption in the relatively homogeneous host rock. The positions of source and receiver are derived

165 from the borehole trajectories, based on the known depth of the sensors along the borehole. The apparent velocities (referred to as ray velocities in the following) must be evaluated with respect to their propagation direction to obtain information on the anisotropy of a medium. In Fig. 3 all source-receiver combinations are plotted as dots in a stereonet representation, colored based on the velocity along the ray. We follow the geological convention of an azimuth of  $0^\circ$  pointing towards magnetic North, increasing clockwise and a dip of  $0^\circ$  being horizontal, increasing downwards. The stereonet plots show the lower hemisphere representation.

170 The stereonet plots show the angular coverage in the volume that we obtained from our sensor positions, as well as the amount of picks we can determine for the different wave types. With our borehole orientation, we can cover mainly rays with N-S or E-W orientation for most dip directions. Only vertical rays ( $\theta = 90^\circ$ ) and rays in NE-SW and NW-SE orientations can not be covered in our surveys, so that we have no information on the velocities in these directions.

Looking at the color pattern in Fig. 3, a clear trend of faster and slower velocities is recognized for both, P- and S1-waves. Waves with E-W



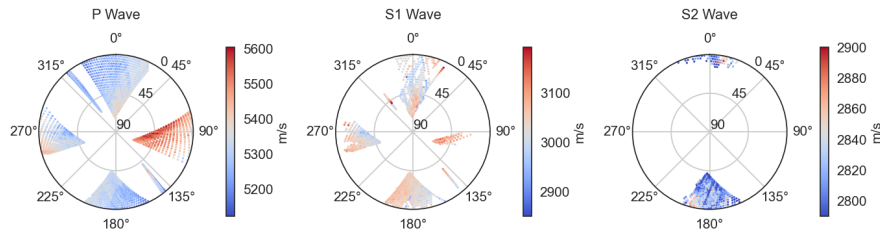


**Figure 3.** The stereonets show the apparent velocities of the three wave types, calculated based on the sensor positions and picked onset times. Each dot represents one source-receiver couple, colored by the apparent velocity of the (a) P-Wave, (b) S1-Wave and (c) S2-wave. The amount of picks decreases as S-Waves can not be picked precisely on all datasets.

175 orientation travel faster than waves perpendicular to it with N-S orientation. The maximum of the P-wave velocity can be found in the right triangle, corresponding to rays in the plane between SB2.1 and SB2.2. Likewise, a trend of increasing velocities in clockwise direction can be found for rays in plane SB2.2 to SB2.3 (upper and lower triangle) with minimum velocities in NNW-SSE orientation, perpendicular to the maximum velocity direction. While these trend is quite strong for P-waves, a similar but less dominant trend can also be observed for S1-waves.

180 In the velocity pattern of the S2-waves no clear trend of a velocity change is visible. However, only for certain ray directions a splitting of S-waves can be detected. Different types of S-waves can only be detected in N-S direction, while the S-waves are not clearly separated in E-W direction. In general, the amount of clearly identifiable arrivals decreases from P- over S1- to S2-waves.

As mentioned in Sect. 4, the 3C geophone data were used to verify the recordings on the hydrophones. The arrival times of P- and S1-waves were also picked on the 3C geophones and plotted in a stereonet plot. The result is shown in Fig. A3. The velocity pattern matches the pattern

185 of the hydrophone data in Fig. 3, but the data quality is lower so that less picks are available and higher uncertainties are expected. Based on the variation of the measured data, the anisotropy factor can directly be calculated by  $(v_{\max} - v_{\min})/v_{\text{mean}}$ . It is describing the variation of the velocities, indicating how much they differ with respect to the propagation directions. Instead of using the maximum and minimum velocities, we used the average of the highest and lowest 5% of the data to avoid a distortion of the result by outliers. For the P-waves an anisotropy of 6.4% is determined, S1-waves show an anisotropy of 5.1%. However, for both wave types the real value might be

190 even higher as not all ray directions can be measured and the maximum or minimum velocities might be missed. We are aware that also uncertainties in the borehole trajectories and thus in the source and receiver positions can mimic anisotropy in an intrinsically isotropic rock (Maurer and Green, 1997). The fact that we can detect shear wave splitting for some ray directions, as well as the highly precise measurements of the borehole trajectories preclude the option of wrongly assuming anisotropy in our rock volume.

## 6 Results

195 In Sect. 5, we already mentioned that the picked traveltimes of the measured seismic signals show the expected velocity pattern of a TTI medium. Now we explain the measured data with an anisotropic velocity model defined by the Thomsen parameters to identify the potential sources causing the seismic anisotropy. Also the sensitivities of the model parameters needs to be analysed to understand the reliability of the model.

In a first step, a grid search over the whole parameter space for  $\phi_0$  and  $\theta_0$  and the relevant parameter values for  $\epsilon$  and  $\delta$  was used to determine





200 a set of parameters describing the P-wave data. After the first run, a second grid search with refined grid spacing close to the best fitting parameters was performed. The values of  $\alpha_0 = 5115 \text{ m s}^{-1}$  was kept fixed for both runs, based on values from previous measurements (Schneider, 2022).

The refined grid search results were further improved by a downhill simplex algorithm, minimizing the root-mean-square error (RMS)

**Table 3.** The table shows both, the parameter range of the grid searches ([start value, end value, step size]) and initial values of the optimization as well as the optimized parameter sets after (a) the general grid search over the whole parameter space, (b) the refined grid search around the optimum of (a) and (c) the optimization algorithm. The last column shows the root-mean square error of the P-waves for the grid search and the weighted root-mean square error of all wave types for the optimization algorithm. All values are in the respective units.

Parameter Space (a and b) and Initial Guess (c)	Optimized Parameter	RMS
	$[\varphi_0, \theta_0, \epsilon, \delta]$ $[\alpha_0, \beta_0, \gamma]$ (for (c))	
<b>(a) General Grid Search [min, max, step size]</b> $\varphi_0$ : [180°, 360°, 1°], $\theta_0$ : [0°, 90°, 1°] $\epsilon$ : [0, 0.3, 0.02], $\delta$ : [-0.2, 0.2, 0.02]	[344°, 10°, 0.06, 0.16]	68.51
<b>(b) Refined Grid Search [min, max, step size]</b> $\varphi_0$ : [342°, 346°, 0.1°], $\theta_0$ : [8°, 12°, 0.1°] $\epsilon$ : [0.04, 0.08, 0.01], $\delta$ : [0.14, 0.18, 0.01]	[344.3°, 10°, 0.06, 0.15]	68.18
<b>(c) Optimization Algorithm</b> $\varphi_0 = 344.3^\circ$ , $\theta_0 = 10.0^\circ$ $\epsilon = 0.06$ , $\delta = 0.15$ $\alpha_0 = 5115 \text{ m s}^{-1}$ , $\beta_0 = 2840 \text{ m s}^{-1}$ , $\gamma = 0.09$	[323.20°, 17.85°, 0.038, 0.047] [5221 $\text{m s}^{-1}$ , 2852 $\text{m s}^{-1}$ , 0.101]	54.38

205 between the modeled and measured velocities of all three wave types. The RMS of the different wave types was weighted to take the uncertainty of the different S-waves into account. The RMS of the P-waves was weighted higher with a value of 0.6, while S1- and S2-waves are weighted by 0.3 and 0.1, respectively. The parameter space and results of the grid search and optimization algorithm are summarized in Tab. 3.

210 Additionally, a sensitivity analysis was carried out to investigate the reliability of the optimized parameters. This is particular important for the deeper understanding and interpretation of the optimized model. The model resolution matrix of all three wave types individually as well as a matrix combining all three wave types is analysed to highlight the importance of combining information from all three wave types to fully describe the elastic tensor of the rock.

### 6.0.1 Sensitivity Analysis

215 The results of the sensitivity analysis are shown in Fig. 4 for the analysis of the single wave types (a-c) and the combination of all wave types (d). In the matrix itself, the values as well as the colors are normalized by the diagonal element of each row to show the trade-off between the different parameters. The column on the left represents the absolute values of the diagonal entries of the matrix for each parameter to show how well the parameter can be resolved based on our setting. White diagonal elements mean that the wave type does not provide any information on this parameters. White colors on the off-diagonal mean that there is (almost) no trade-off between the parameters (normalized

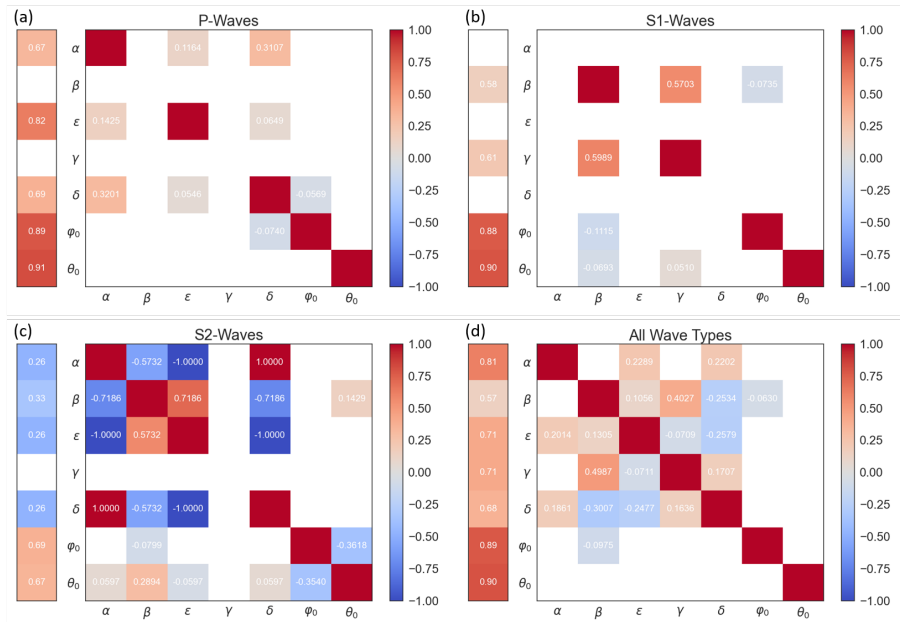


**Figure 4.** The model resolution matrices, using only one wave type((a): P waves, (b) S1 waves, (c) S2 waves) and combining the information of all three wave types (d). The column on the left shows the relative difference of the diagonal elements while the values in the matrix are normalized for each row by the diagonal element.

values between -0.05 and +0.05 are also plotted in white to simplify the matrix).

Matrices (a) to (c) directly show, that none of the wave types can provide information on all seven parameters describing the elastic properties of the rock volume. While all wave types provide information on the orientation of the symmetry axis ( $\varphi_0$  and  $\theta_0$ ), each wave type contains only information about a subset of the Thomsen parameters. The matrices further show that the orientation of the symmetry axis is highly constrained, even if only one wave type is used in the analysis. This is expected, as we can cover many different ray directions with our borehole orientation.

If only P-wave data are used to model the anisotropy, information on  $\beta$  and  $\gamma$  are completely missed. Combining the information of P-waves with the traveltimes of S1-waves can close this gap and fully describe all parameter as the different waves contain complementary information. The S1-wave is not controlled by  $\delta$ , so that also the trade-off between  $\varphi_0$  and  $\delta$ , which is present for P-waves, can be eliminated by adding the S1-wave data to the model.

The absolute velocities of the waves along the axis, represented by  $\alpha$  and  $\beta$  are slightly affected by the parameters  $\epsilon$ ,  $\delta$  and  $\gamma$  for P- and S1-waves. Fig. 4(a) also shows a slight trade-off between  $\epsilon$  and  $\delta$ , however this trade-off is negligible small. The small trade-offs between the different parameters are also apparent in the diagonal element values shown in the left column. Both angles have a value of about 0.9, showing that they are highly constrained by our data. The other parameters of both, P- and S1-waves, are mostly larger than 0.6, indicating that also these parameters are acceptable but still less constrained. Only  $\beta$  is slightly lower for S1-waves, as a stronger trade-off with  $\gamma$  is present.

The matrix of the S2-waves (Fig. 4(c)) shows a different behaviour. S2-waves contain information of almost all parameters, only  $\gamma$  is not

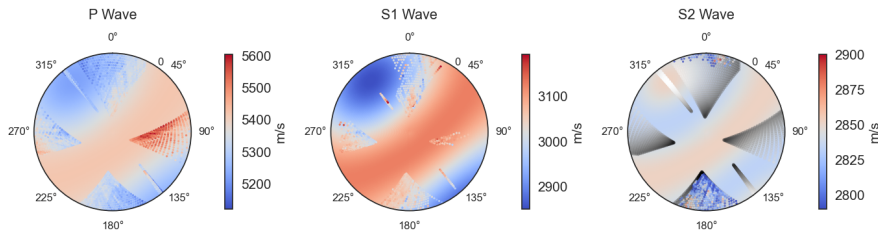


**Figure 5.** The background color shows the apparent velocities for the (a) P-Wave, (b)SH-Wave and (c) SV-Wave based on the optimized model. Dots in the foreground represent the measured apparent velocities for the covered ray directions. In (c) the difference of the traveltimes from the SH- and SV-Waves are additionally shown in grey for all measured data points.

235 controlling the S2-wave velocity.

As before, the orientation of the symmetry axis has the highest absolute values and indicates the least correlation to other parameters. However, the Thomsen parameter show a very high trade-off between each other. Especially the contrary influence of  $\delta$  and  $\epsilon$  on  $\alpha$  leads to inconclusive information on these parameters, as errors in one parameter might be compensated by the other parameter. The different parameters cannot be resolved independently, resulting in very low constrained absolute values for all Thomsen parameters including the velocities  $\alpha$  and  $\beta$ . Nevertheless, also information of the S2-wave velocity should be included in the final model to avoid artificially constraining the final model.

In Fig. 4(d), the model resolution matrix  $\mathbf{R}$  for the combined analysis of all three wave types is shown. Combining the information of all wave types results in a highly constrained model for all seven unknowns of a TTI model. The orientation of the symmetry axis has, as for all single wave information, no significant trade-off with any other parameters. Most of the other parameters show a small trade-off between each other with absolute values smaller-equal than 0.3, except from  $\beta$  to  $\gamma$ . The high diagonal elements for all parameters indicate that we can have a high confidence in the accuracy of the optimized parameters.

The higher trade-off between  $\beta$  and  $\gamma$  results from the fact that  $\gamma$  is only controlling the wave propagation of the S1-wave, so that the other wave types can not compensate this trade-off, as it is the case for other parameter combinations. More measurement points of the S1-wave could help to improve this correlation, however the S1-wave is partly covered by the coda of the P-wave or tube and reflection waves, which makes an accurate determination of the travel time in some directions impossible.

## 6.0.2 Analysis of the model fit

The result of the optimized model in comparison with the measured data are shown in Fig. 5. The background color shows the velocity distribution based on the optimized parameters from Tab. 3(c), while the dots in the foreground show the actually measured data. The color range for both, the measured and optimized data is the same, so that measurement points which are hard to distinguish from the background represent a high accordance with the optimized model. In the right plot for the S2-waves, the expected travel time *difference* between the S1- and S2-wave is shown in grey, with light colors for a small difference and darker colors for a higher difference.

The optimized model fits the pattern of the measured data of the P- and S1-waves quite well. This further confirms our assumption of a TTI medium. While the maximum magnitude of the P-waves is slightly underestimated, the magnitude of the S1-wave is in good accordance with the optimized model. Especially the trend of increasing velocities away from the symmetry axis at  $\varphi_0 = 323.20^\circ$ ,  $\theta_0 = 17.85^\circ$  towards

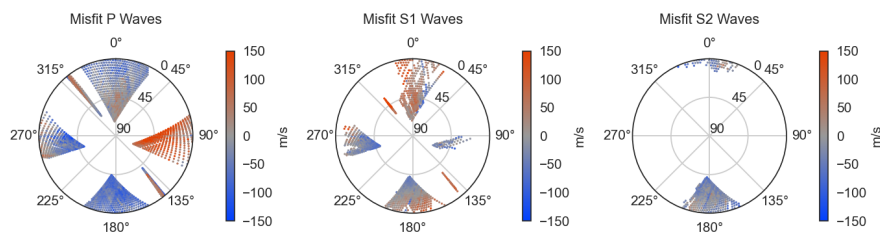


**Figure 6.** The stereonet shows the misfit between the optimized model and the measured apparent velocity for all picked data. The range of the colorbar is equalized for a better comparison of the misfits. A negative misfit means that the optimized model is overestimating the velocity.

260 the symmetry plane perpendicular to it, mainly visible in the upper and right triangle, fits very well to the measured velocities. S2-waves can only be picked in the plane between borehole SB2.2 and SB2.3. In this plane, less interference with other wave types is disturbing the signal and the travelt ime difference between the S1- and S2-waves is large enough to separate the waves. This fits at least partly to the expected travelt ime difference, shown in grey colors in the Fig. 5. In white parts, where the expected travelt ime difference is close to 0, no splitting of the waves was detected while for most parts with larger travelt ime difference (dark), two different S-wave arrivals  
 265 can be picked. In general, the measured S2-wave velocities do not show a strong velocity change with the ray direction but only small amplitude variations from  $2800 \text{ m s}^{-1}$  up to  $2900 \text{ m s}^{-1}$ .

Analogous to the anisotropy factor based on the measured data, the anisotropy factor can also be calculated for the model data. The P-waves show an anisotropy of 3.5% in the optimized model, the S1-waves show an anisotropy of 6.6%. These values are in the same order of magnitude as the anisotropy factors of the measured data in Sect. 5.

270 Even though the optimized TTI model can explain the measured data to a first order, it still shows a systematic misfit, shown in Fig. 6. The representation is the same as before, but the color refers to the absolute misfit for each ray direction. The maximum, absolute misfit of all wave types is in the range of about 200 m/s, which corresponds to an offset of about 3 - 7%. This shows, that the final anisotropic velocity model explains the measured data reasonable.

The misfit shows trends of over- and underestimated velocities for P- and S1-waves. For P-waves, velocities in EW-directions are mainly  
 275 underestimated, while rays with NS-orientation are overestimated by the model. The error of the S1-waves shows a less dominant pattern, but is still not randomly distributed and shows underestimated velocities for mainly horizontal rays and rays in NW-SE direction such as overestimated velocities for steeper ray directions. The model overestimates the S2-wave velocities for most ray directions. It is also remarkable that the shear wave splitting is mainly detected in parts, where the P-wave velocity is overestimated, while the S1-wave velocity is underestimated. A model with a higher fit in these parts could potentially result in a higher expected travelt ime difference than assumed  
 280 by our model, fitting to a splitting in these parts.

While such a systematic error is an indicator of an inadequate assumption in the model, the overall fit of our model is still adequate and it can be used for further characterizations of the rock volume. Potential sources for the observed anisotropy are discussed in the following Sect. 7 by comparing our results to other studies.



## 7 Discussion

285 The picked traveltimes of the P-waves give evidence for seismic anisotropy in the volume of interest, which can by first order be described as a TTI model. This symmetry is further confirmed by the two different shear waves following matching patterns. The high angular coverage in the tripod boreholes as well as the large amount of picked arrival times for all three wave types allow us to determine a well-constrained anisotropic velocity model.

While it is common to analyze the seismic anisotropy of a rock on the lab scale (David et al., 2020; Schneider, 2022; Sayers, 2002; Nur  
290 and Simmons, 1969) and for rock types other than igneous rocks (Al-Harhi, 1998; Chan and Schmitt, 2015; Song et al., 2004), it is often not taken into account on the field scale for igneous rocks. This can not only lead to flawed results in the velocity model but also important information on the rock characteristics are neglected.

The analysis of seismic anisotropy on the field scale offers significant advantages over lab-scale experiments. While measurements in the laboratory give only insights on the features of the undisturbed rock, also fractured or brittle material can be tested on the field scale. It is  
295 known that open and filled fractures are crossing the volume of interest, potentially influencing the wave propagation in our test bed. These effects are missed in lab-scale experiments.

Another advantage is the interpretation of the result in a larger context. The laboratory can only offer quantitative information about the elastic tensor but not about the orientation of it in the field. However, the orientation of the tensor, described by the symmetry axis, is of high importance to identify the causative factors of anisotropy. Not only the orientation of the sample but also the in-situ conditions can not be  
300 preserved in the laboratory. During the exhumation of the rock, a non-reversible relaxation of the sample occurs, altering the external forces that control its elastic properties.

In the following, we consider various factors that may control anisotropy, and we discuss how adequate they can describe our measured anisotropy.

Different factors are known to cause seismic anisotropy on different scales (Barton, 2006):

- 305 – Interbedding of sedimentary rocks
- Fault zones
- Fabrics
- Natural Fractures
- Stress Field Orientation

310 The first two factors can be eliminated in our rock volume, as the tripod is placed in an undisturbed part of the Rotondo granite. Different logging runs proved that the boreholes are not crossing any major fault zones or larger fracture zones. The seismic data have also no indication for larger heterogeneities within the test volume, which is in good accordance with the geological characterization of Jordan (2019). The fabrics of the rock can also be excluded as potential source as the thin sections and core samples of the undisturbed granite don't show any preferred orientation or mineral alignment (David et al., 2020; Ma et al., 2022; Jordan, 2019). The undeformed Rotondo granite is also  
315 fully isotropic under high pressures in the lab, indicating that the anisotropy is not intrinsic from the material itself but must be controlled by external factors (Schneider, 2022). Under high pressure all cavities are closed, so that a preferred orientation of the minerals would cause anisotropic velocities.

The remaining factors which are known to cause anisotropy are (natural) fractures and the predominant stress field in the rock volume. The occurrence and orientation of the fractures in the tripod boreholes are analyzed in Bröker et al. (2024). Jordan (2019) additionally mapped



320 fractures along the tunnel wall. The results of both studies are summarized in Fig. 7. Black lines represent the strike direction of mapped fractures along the tunnel and turquoise lines represent the strike direction of the mapped fractures of the logging data.

The fractures mapped in the tunnel show a slight trend of NS-striking fractures around the tripod boreholes which is supplemented by NW-SE striking fractures in the logging data. The NW-SE striking fractures are undersampled in the tunnel wall mapping, due to their subparallel orientation to the tunnel. This means that the data set based on the logging data is assumed to be more representative for our rock volume. In  
325 both data sets, the fractures are mainly sub-vertical. The fractures mapped in the borehole are mainly dipping towards east or south-east, the fractures mapped along the tunnel wall do not show a dominant dip direction.

However, in addition to the fractures, also stress-induced anisotropy is a possible source for the measured anisotropy in the tripod. The magnitude and orientation of the stress field around the tripod is analysed in Bröker and Ma (2022) and Bröker et al. (2024), respectively. They state that one of the principal stress components is vertically oriented ( $S_v$ ) and in the same order of magnitude as the maximum horizontal  
330 stress ( $S_{HMax}$ ), pointing in  $N75^\circ E$  to  $N87^\circ E$  direction around the tripod boreholes. The orientation of  $S_{HMax}$ , estimated from mini-frac tests, is also plotted in Fig. 7 by the black arrows.

Comparing the orientation of the fractures and the in-situ stress field with the orientation of the anisotropy can reveal information about the correlation between the different characteristics. In the case of a purely fracture-dominated anisotropy, we would assume faster velocities along the fractures and minimum wave velocities perpendicular to it (Barton, 2006). In the tripod, this would correspond to faster velocities  
335 in a vertical plane with N-S to NW-SE orientation and a symmetry axis in E-W to NE-SW direction. In the case of a purely stress-induced anisotropy, faster wave velocities are expected along the maximum principle stress direction (Nur and Simmons, 1969; Barton, 2006; Song et al., 2004). This means that in the case of  $S_v \approx S_{HMax}$ , the seismic velocities are not just maximized in one specific direction but within the plane spanned by the two maximum stress directions. In the case of the tripod, this plane is oriented in E-W to NE-SW direction.

In Fig. 7 the relations between the fracture network (lines in black and turquoise), the stress field (black arrows) and the symmetry plane of  
340 maximum velocities (red) are summarized. The symmetry plane with maximum velocities is rather aligned with the maximum stress directions than with the preferred orientation of fractures in the tripod. Also the velocity pattern corresponding to a mostly rotational symmetric TTI medium fits the expectation of a stress-induced anisotropy with  $S_v \approx S_{HMax}$ .

However, the orientation of the symmetry plane cannot exclusively be explained by the stress field, which suggests that a combined effect of the fracture network and stress field is controlling the anisotropy in the tripod. Also the systematic distribution of the misfit indicates that the  
345 assumption of a homogeneous TTI medium might be too strong and cannot fully cover our observations. The heterogeneous distribution of filled and unfilled fractures along the boreholes gives more complexity to the velocity field and potentially also reduces the symmetry from a hexagonal TTI medium towards a slightly orthorhombic medium.

Our measurements are not just in accordance with the orientation of the in-situ stress-field but also quantitatively with first lab measurements from David et al. (2020) and Wenning et al. (2018) on the Rotondo granite. They measure a seismic anisotropy of about 6% under zero-  
350 confinement pressure and 30 MPa confinement pressure, respectively. However, in both studies only a limited amount of ray directions was measured, so the maximum and minimum velocity direction might be missed and the true anisotropy might also be higher.

A common explanation for seismic anisotropy on the lab scale is the preferred orientation of so-called micro-cracks in the sample which is controlled by the applied stress-field, closing cracks perpendicular to the maximum stress direction. This effect is not fully reversible so that the samples in the lab still behave anisotropic even without any applied differential pressure.

355 This explanation of the closure of micro-cracks might be true for sedimentary rocks with a significant amount of micro-cracks between the grains. However, micro-cracks are less dominant in igneous rocks so that this effect is assumed to be small (Howarth, 1987). Maitra and Al-Attar (2021) states that the effect of differential stress on a solid medium can rather be explained by a change in the elastic tensor of the

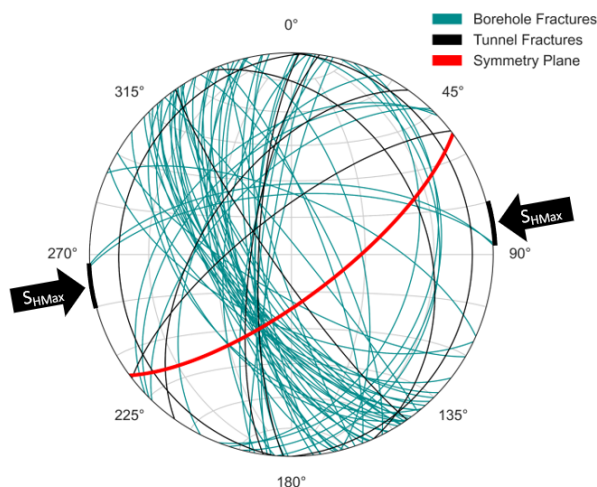


**Figure 7.** The stereonet represents the natural fractures along the tunnel wall from TM 2050m - 2115m (black) and in the boreholes (grey) and the symmetry plane (red) of the optimized anisotropy model. The black arrows point towards  $S_{HMax}$  around the tripod boreholes as estimated from mini-frac tests by Bröker et al. (2024).

effective medium than by the effect on its cavities. The elastic tensor is affected by the in-situ stress field with three distinct principal stresses, causing a higher stiffness of the material along  $\sigma_{max}$ , increasing the wave velocity along it.

360 It is known, that also uncertainties in the borehole trajectory can cause a comparable velocity pattern, mimicking seismic anisotropy or change the TTI model (Maurer and Green, 1997; Hellmann et al., 2023). The velocity pattern based on an earlier and less accurate trajectory calculation is shown in Fig. A4. It shows a similar but rotated velocity pattern with faster velocities in NE-SW direction, rather than in E-W direction. This further demonstrates that the anisotropy model is highly sensitive to errors in the boreholes trajectories.

365 However, the occurrence of the splitting of the two differently polarized S-wave is a clear evidence for true seismic anisotropy in the volume of interest. Additionally, the trajectories of the boreholes used in this study are known with up to a millimeter precision. This allows the determination of a reliable final model which can be used for further analyses on the source of the anisotropy. The relation between borehole trajectories and seismic anisotropy calculations will be analysed in more detail in an upcoming study.

## 8 Conclusions

370 The cross hole seismic data set measured in the tripod boreholes of the Bedretto Lab allow a reliable determination of a TTI model. We were able to measure wave velocities in a large range of directions, covering most azimuth and dip directions. The detection of the different wave types (P-, S1- and S2-waves) further constrains the velocity model as the wave velocities contain supplementary information of the elastic tensor. The most likely cause of the anisotropy is a combination of the stress field and the fracture network. The stress field can explain the main features of the velocity distributions, with a rotational symmetric pattern around the symmetry axis pointing towards the minimum stress direction. However deviations from this TTI model, which become particularly evident in the systematic misfit, can be assigned to the





375 orientation of the fractures in the volume. A more complex model with a lower (orthorhombic) symmetry could potentially account for these effects but the lack of data especially within the symmetry plane makes a reliable calculation of an orthorhombic medium impossible.

*Data availability.* All data used in this project are available through <https://doi.org/10.3929/ethz-b-000678987>

*Author contributions.* KBe, MH, CE and MBL conducted the experiments; KBe, CE and MBL processed and analysed the data; KBe, KBr, 380 MH and HM interpreted the results in the bigger context of the BedrettoLab; AS provided and updated the borehole trajectories, KB wrote the paper with contributions from all co-authors.

*Competing interests.* The authors declare that they have no conflict of interest.

*Acknowledgements.* In the "Bedretto Underground Laboratory for Geosciences and Geoenergies", ETH Zurich studies in close collaboration with national and international partners techniques and procedures for a safe, efficient, and sustainable use of geothermal heat and questions 385 related to earthquake physics. The BedrettoLab is financed by the Werner Siemens Foundation, ETH Zürich and the Swiss National Science Foundation. The research in this publication was conducted within the project 200021\_192151 and has received funding by the Swiss National Science Foundation (SNF). The BedrettoLab would like to thank Matterhorn Gotthard Bahn for providing access to the tunnel. This paper is BULGG publication BPN\_026.



## Appendix A: Additional Plots

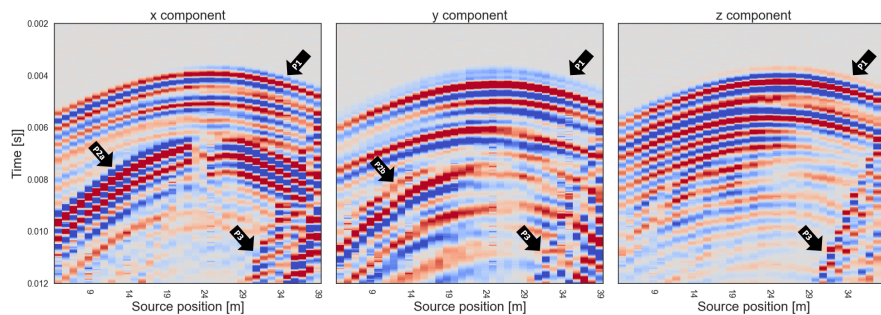


**Figure A1.** The receiver gathern for the same geometry as in Fig. 2 recorded on a 3C geophone (Receiver in SB2.2 at 23m depth, source in SB2.3 with 1m spacing). The P-wave arrival is clearly visible (P1). On the x-component, the arrival of the S1-wave is visible (P2a), the onset recorded on the y-component is slightly later and thus, corresponds to the S2-wave (P2b). On the z-component, no S-wave signal is recorded. All components also contain reflected or tube waves (P3).

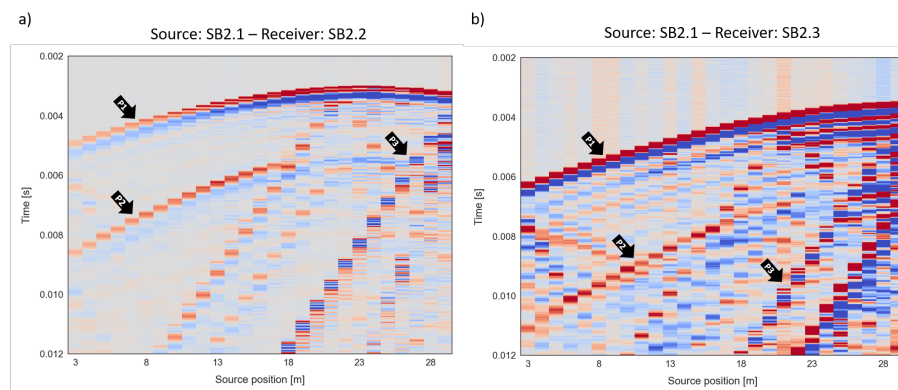


**Figure A2.** (a) Shot Gathern of a source in borehole SB2.1 at 26m depth, recorded on hydrophones in SB2.2 with 1m spacing. (b) Shot Gathern of a source in borehole SB2.1 at 32m depth, recorded on hydrophones in SB2.3 with 1m spacing. Arrows point to the P-wave arrival (P1), S1-wave arrival (P2) and reflected or tube waves (P3). In both geometries, no clear splitting of the S-waves is detected.

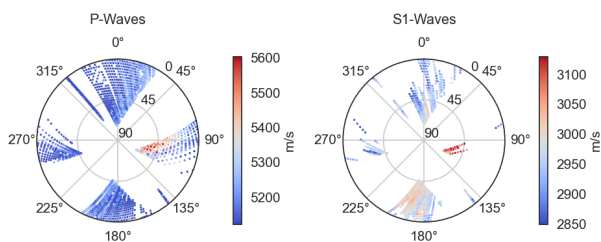


**Figure A3.** Calculated apparent velocities based on the picked traveltimes on the 3C geophones. The overall pattern fits the velocity pattern of the hydrophone data set, but the magnitudes are smaller compared to the hydrophone dataset. Problems in the data acquisition, triggering the recording, can explain this shift.

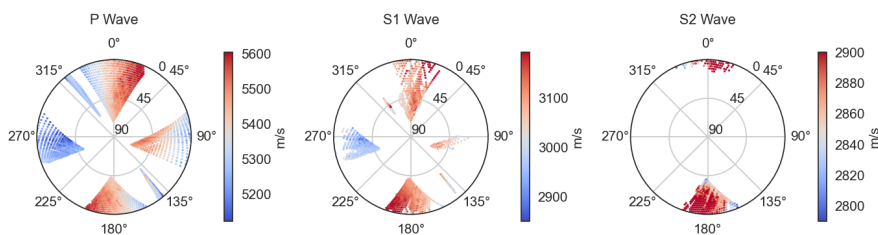


**Figure A4.** Apparent velocities for all three wave types, based on the old trajectories. These trajectories have a higher uncertainty as they are purely based on logging information.



## 390 References

- Al-Harathi, A. A.: Effect of planar structures on the anisotropy of Ranyah sandstone, Saudi Arabia, *Engineering Geology*, 50, 49–57, [https://doi.org/10.1016/S0013-7952\(97\)00081-1](https://doi.org/10.1016/S0013-7952(97)00081-1), 1998.
- Amann, F., Gischig, V., Evans, K., Doetsch, J., Jalali, R., Valley, B., Krietsch, H., Dutler, N., Villiger, L., Brixel, B., Klepikova, M., Kittilä, A., Madonna, C., Wiemer, S., Saar, M. O., Loew, S., Driesner, T., Maurer, H., and Giardini, D.: The seismo-hydromechanical behavior during deep geothermal reservoir stimulations: Open questions tackled in a decameter-scale in situ stimulation experiment, <https://doi.org/10.5194/se-9-115-2018>, 2018.
- Barton, N.: *Rock quality, seismic velocity, attenuation and anisotropy*, CRC press, ISBN 1134160135, 2006.
- Bröker, K. and Ma, X.: Estimating the Least Principal Stress in a Granitic Rock Mass: Systematic Mini-Frac Tests and Elaborated Pressure Transient Analysis, *Rock Mechanics and Rock Engineering*, 55, 1931–1954, <https://doi.org/10.1007/s00603-021-02743-1>, 2022.
- 400 Bröker, K., Ma, X., Zhang, S., Gholizadeh Doonechaly, N., Hertrich, M., Klee, G., Greenwood, A., Caspari, E., and Giardini, D.: Constraining the stress field and its variability at the BedrettoLab: Elaborated hydraulic fracture trace analysis, *International Journal of Rock Mechanics and Mining Sciences*, 178, 105 739, <https://doi.org/10.1016/J.IJRMMS.2024.105739>, 2024.
- Carcione, J. M., Kosloff, D., and Kosloff, R.: Wave-Propagation Simulation in an Elastic Anisotropic (Transversely Isotropic) Solid, *The Quarterly Journal of Mechanics and Applied Mathematics*, 41, 319–346, <https://doi.org/10.1093/qjmam/41.3.319>, 1988.
- 405 Chan, J. and Schmitt, D. R.: Elastic Anisotropy of a Metamorphic Rock Sample of the Canadian Shield in Northeastern Alberta, *Rock Mechanics and Rock Engineering*, 48, 1369–1385, <https://doi.org/10.1007/s00603-014-0664-z>, 2015.
- Daley, P. F. and Hron, F.: Reflection and transmission coefficients transversely isotropic media, *Tech. Rep. 3*, <http://pubs.geoscienceworld.org/ssa/bssa/article-pdf/67/3/661/5320942/bssa0670030661.pdf>, 1977.
- David, C., Nejati, M., and Geremia, D.: On petrophysical and geomechanical properties of Bedretto Granite, *Tech. rep.*, 2020.
- 410 Eken, T., Plomerová, J., Vecsey, L., Babuška, V., Roberts, R., Shomali, H., and Bodvarsson, R.: Effects of seismic anisotropy on P-velocity tomography of the Baltic Shield, *Geophys. J. Int.*, 188, 600–612, <https://doi.org/10.1111/j.1365-246X.2011.05280.x>, 2012.
- Geotomographie GmbH: <https://geotomographie.de/equipment/borehole-sources>, accessed: 2024-06-03.
- Gischig, V. S., Giardini, D., Amann, F., Hertrich, M., Krietsch, H., Loew, S., Maurer, H., Villiger, L., Wiemer, S., Bethmann, F., Brixel, B., Doetsch, J., Doonechaly, N. G., Driesner, T., Dutler, N., Evans, K. F., Jalali, M., Jordan, D., Kittilä, A., Ma, X., Meier, P., Nejati, M., Obermann, A., Plenkers, K., Saar, M. O., Shakas, A., and Valley, B.: Hydraulic stimulation and fluid circulation experiments in underground laboratories: Stepping up the scale towards engineered geothermal systems, *Geomechanics for Energy and the Environment*, 24, 100 175, <https://doi.org/10.1016/J.GETE.2019.100175>, 2020.
- 415 Hellmann, S., Grab, M., Patzer, C., Bauder, A., and Maurer, H.: A borehole trajectory inversion scheme to adjust the measurement geometry for 3D travel-time tomography on glaciers, *Solid Earth*, 14, 805–821, <https://doi.org/10.5194/se-14-805-2023>, 2023.
- 420 Heng, S., Guo, Y., Yang, C., Daemen, J. J., and Li, Z.: Experimental and theoretical study of the anisotropic properties of shale, *International Journal of Rock Mechanics and Mining Sciences*, 74, 58–68, <https://doi.org/10.1016/J.IJRMMS.2015.01.003>, 2015.
- Horne, S. A.: A statistical review of mudrock elastic anisotropy, *Geophysical Prospecting*, 61, 817–826, 2013.
- Howarth, D. F.: The effect of pre-existing microcavities on mechanical rock performance in sedimentary and crystalline rocks, *International Journal of Rock Mechanics and Mining Sciences & Geomechanics Abstracts*, 24, 223–233, [https://doi.org/10.1016/0148-9062\(87\)90177-](https://doi.org/10.1016/0148-9062(87)90177-X)
- 425 X, 1987.



- Jordan, D.: Geological Characterization of the Bedretto Underground Laboratory for Geoenergies, <https://doi.org/10.3929/ethz-b-000379305>, 2019.
- Keller, F. and Schneider, T. R.: *Geologie und Geotechnik*, Schweizer Ingenieur und Architekt, 100, 512–520, 1982.
- Lee, H., Ong, S. H., Azeemuddin, M., and Goodman, H.: A wellbore stability model for formations with anisotropic rock strengths, *Journal of Petroleum Science and Engineering*, 96-97, 109–119, <https://doi.org/10.1016/J.PETROL.2012.08.010>, 2012.
- Ma, X., Hertrich, M., Amann, F., Bröker, K., Gholizadeh Doonechaly, N., Gischig, V., Hochreutener, R., Kästli, P., Krietsch, H., Marti, M., Nägeli, B., Nejati, M., Obermann, A., Plenkers, K., Rinaldi, A. P., Shakas, A., Villiger, L., Wenning, Q., Zappone, A., Bethmann, F., Castilla, R., Seberto, F., Meier, P., Driesner, T., Loew, S., Maurer, H., Saar, M. O., Wiemer, S., and Giardini, D.: Multi-disciplinary characterizations of the BedrettoLab – a new underground geoscience research facility, *Solid Earth*, 13, 301–322, <https://doi.org/10.5194/se-13-301-2022>, 2022.
- Maitra, M. and Al-Attar, D.: On the stress dependence of the elastic tensor, *Geophysical Journal International*, 225, 378–415, <https://doi.org/10.1093/gji/ggaa591>, 2021.
- Maurer, H. and Green, A. G.: Potential coordinate mislocations in crosshole tomography: Results from the Grimsel test site, Switzerland, *Geophysics*, 62, 1696–1709, <https://doi.org/10.1190/1.1444269>, 1997.
- Menke, W.: *Geophysical data analysis discrete inverse theory*, Academic Press, Amsterdam, fourth edition edn., ISBN 9780128135556, 2018.
- Nur, A. and Simmons, G.: Stress-induced velocity anisotropy in Rock: An Experimental Study, *J Geophys Res*, 74, 6667–6674, <https://doi.org/10.1029/jb074i027p06667>, 1969.
- Özbek, A., Gül, M., Karacan, E., and Alca, : Anisotropy effect on strengths of metamorphic rocks, *Journal of Rock Mechanics and Geotechnical Engineering*, 10, 164–175, <https://doi.org/10.1016/J.JRMGE.2017.09.006>, 2018.
- Plenkers, K., Reinicke, A., Obermann, A., Doonechaly, N. G., Krietsch, H., Fechner, T., Hertrich, M., Kontar, K., Maurer, H., Philipp, J., Volksdorf, M., Giardini, D., and Wiemer, S.: Multi-Disciplinary Monitoring Networks for Mesoscale Underground Experiments: Advances in the Bedretto Reservoir Project, <https://doi.org/10.3390/s23063315>, 2023.
- Ramamurthy, T., Rao, G. V., and Singh, J.: Engineering behaviour of phyllites, *Engineering Geology*, 33, 209–225, [https://doi.org/10.1016/0013-7952\(93\)90059-L](https://doi.org/10.1016/0013-7952(93)90059-L), 1993.
- Rast, M., Galli, A., Ruh, J. B., Guillong, M., and Madonna, C.: Geology along the Bedretto tunnel: kinematic and geochronological constraints on the evolution of the Gotthard Massif (Central Alps), *Swiss Journal of Geosciences*, 115, 8, <https://doi.org/10.1186/s00015-022-00409-w>, 2022.
- Sayers, C. M.: Stress-dependent elastic anisotropy of sandstones, *Geophysical Prospecting*, 50, 85–95, <https://doi.org/10.1046/j.1365-2478.2002.00289.x>, 2002.
- Schneider, C.: *Seismic Velocity Anisotropy and Microstructural Characterization of Ductile Shear Zones in the Rotondo Granite*, Ph.D. thesis, 2022.
- Song, I., Suh, M., Woo, Y. K., and Hao, T.: Determination of the elastic modulus set of foliated rocks from ultrasonic velocity measurements, *Engineering Geology*, 72, 293–308, <https://doi.org/10.1016/J.ENGGEOL.2003.10.003>, 2004.
- Thomsen, L.: Weak elastic anisotropy., *Geophysics*, 51, 1954–1966, <https://doi.org/10.1190/1.1442051>, 1986.
- Wenning, Q., Madonna, C., de Haller, A., and Burg, J. P.: Permeability and seismic velocity anisotropy across a ductile-brittle fault zone in crystalline rock, *Solid Earth*, 2018.